Published in partnership with The University of New South Wales



https://doi.org/10.1038/s41534-024-00915-9

Cavity-assisted resonance fluorescence from a nitrogen-vacancy center in diamond

Check for updates

Viktoria Yurgens ^{1,3}, Yannik Fontana ^{1,3} ⋈, Andrea Corazza¹, Brendan J. Shields^{1,2}, Patrick Maletinsky ^{1,3} & Richard J. Warburton ¹

The nitrogen-vacancy center in diamond is an attractive resource for the generation of remote entangled states owing to its optically addressable and long-lived electronic spin. However, its low native fraction of coherent photon emission, ~3%, undermines the achievable spin-photon entanglement rates. Here, we couple a nitrogen-vacancy center with a narrow extrinsically-broadened linewidth (159 MHz), hosted in a micron-thin membrane, to an open microcavity. The resulting Purcell factor of ~1.8 increases the zero-phonon line fraction to over 44%. Operation in the Purcell regime, together with an efficient collection of the zero-phonon-line photons, allows resonance fluorescence to be detected for the first time without any temporal filtering. We achieve a >10 signal-to-laser background ratio. This selective enhancement of the center's zero-phonon transitions could increase spin-spin entanglement success probabilities beyond an order of magnitude compared to state-of-the-art implementations, and enable powerful quantum optics techniques such as wave-packet shaping or all-optical spin manipulation.

The nitrogen-vacancy center (NV) in diamond in its negatively charged state (NV $^-$) offers a direct link between its long-lived spin ground state $^{1-3}$ and photons thanks to spin-conserving optical transitions 4,5 . Spin manipulation via microwaves and optical spin initialization and readout complete the picture of an attractive solid-state spin qubit 6 . However, the NV $^-$'s small optical dipole moment, the high refractive index of diamond, and a $\sim\!\!3\%$ zero-phonon line (ZPL) to phonon side-band (PSB) branching ratio (Debye-Waller factor) preclude the generation of spin-photon entanglement at high rates $^{7-10}$.

A strategy to increase the coherent photon flux involves embedding the NV $^-$ in an optical cavity. Compared to photonic structures designed to improve the collection efficiency, such as solid immersion lenses (SILs) 11,12 , the Purcell effect induced by the cavity additionally increases the fraction of coherent photons. Early attempts at using nanophotonic resonators (e.g., photonic crystals) collided with the detrimental impact of nanofabrication on the optical properties of the NV $^{-13-15}$. An elegant way to overcome this challenge is to place a minimally processed NV $^-$ -containing diamond membrane inside an open microcavity $^{16-19}$. The microcavity offers efficient mode-matching to external optics, optimal positioning of the emitter, and the ability to tune to and selectively enhance specific optical transitions $^{20-29}$.

A spin-photon interface based on a single NV⁻ coupled to a microcavity presents certain challenges: success hinges on simultaneously retaining low cavity losses and a narrow NV $^-$ linewidth. So far, attempts have been partially foiled either by non-optimal cavity performance or by excessive fabrication-induced broadening of the NV ZPL linewidth ^{18,19}. While at room temperature, a cavity finesse—inversely proportional to the round trip losses—of at most 17,000 ¹⁶ has been achieved, the necessary transition to cryogenic temperatures (< 10 K) needed to prevent phonon-induced dephasing generally leads to reduced cavity performance, with a recent implementation yielding a finesse of 12 000^{30} , albeit for a dense and inhomogeneously broadened ensemble. Until now, the various degrees of Purcell-enhancement of a single NV $^-$ emission mostly amounted to values well below unity ^{17,19}. Successful attempts at obtaining significant Purcell factors have fallen short in efficiently extracting the emitted photons, due to intra-cavity losses dominating the optical decay process ¹⁸.

In addition, maintaining high single-photon purity and high indistinguishability requires that the relevant NV $^-$ transitions are excited resonantly, raising the challenge of filtering fluorescence photons from the laser background. So far, robust simultaneous resonant excitation and collection of the ZPL has relied mainly on SILs to increase the collection efficiency and reduce the laser background, backed by polarization-based suppression and systematic temporal filtering of the ZPL photons^{7,8,19}. While temporal filtering offers signal-to-laser background ratio (SLR) of up to $10^{3.8,9,31}$, it also leads to photon-discarding losses. For a Purcell-enhanced NV $^-$, the

¹Department of Physics, University of Basel, 4056 Basel, Switzerland. ²Present address: Quantum Network Technologies, Boston, MA, 02215, USA. ³These authors contributed equally: Viktoria Yurgens, Yannik Fontana. —e-mail: yanniklaurent.fontana@unibas.ch

Fig. 1 | A single NV $^-$ coupled to cavity modes. a Schematic of the tunable open microcavity and diamond membrane. For a cavity frequency matching the ZPL of an NV $^-$, a coherent exchange with coupling strength g_{ZPL} takes place between the NV $^-$ and the optical mode. Concurrently, the NV $^-$ decays into the quasi-free-space continuum at a rate y_0 while the intra-cavity field leaks out of the cavity at a rate κ . b Spectral map over modes 17 to 15. Upon non-resonant excitation, background

photoluminescence from the diamond reveals the mode structure. c Close to resonant conditions, the NV^- selectively couples to the non-degenerate cavity modes M1 and M2 (m_{16} , log scale). d Second-order autocorrelation performed on resonance with mode M1 confirms the isolation of a single NV^- . The data (including background) is fitted with a three-level rate equations model (inset).

shortened lifetime increases the temporal overlap between the NV $^-$ fluorescence and the excitation pulse. This counteracts the improved ZPL photon emission probability. Considering a realistic 2 ns laser π -pulse 8 , the likelihood to detect a ZPL photon in the collection time-window (i.e., after the pulse) decreases for Purcell factors \gtrsim 3, curtailing the benefits of the cavity.

In this work, we couple a low-charge-noise NV^- to the mode of a high-finesse open microcavity at cryogenic temperature. We record Purcell-enhanced ZPL count rates far surpassing current state-of-the-art photonic interfaces based on SILs. Furthermore, polarization-based suppression of the resonant excitation light allows the NV^- cavity-assisted resonance fluorescence (CRF) to be detected without relying on temporal filtering, establishing the platform as an efficient photonic interface for quantum applications.

Results

Single NV coupling and Purcell enhancement

The open microcavity, schematically represented in Fig. 1a, consists of a planar bottom mirror and a curved top mirror (radius of curvature ~14 µm). Both mirrors are distributed Bragg reflectors (DBRs) with reflectivities aiming at a design finesse of 11 614. Excitation and collection are performed through an objective via the top mirror, with transmission $\mathcal{F}_{top} \sim 10 \cdot \mathcal{F}_{bottom}$. The asymmetry in mirror reflectivities results in a one-sided cavity with a decay rate κ and ensures that photons emitted out of the cavity are preferentially collected by the objective. The diamond, a 1.6 µm-thick membrane, is bonded to the bottom mirror via van der Waalsforces ^{16,18}. It contains NV $^-$ created by carbon implantation post-fabrication, a method developed to yield low-noise NV $^-$ centers in microstructures (specifically sample B in ref. 32). A coupled NV $^-$ radiates into free space at a natural rate y_0 while concurrently exchanging energy at a rate $g_{\rm ZPL}$ with a resonant cavity mode.

Using the positioning flexibility offered by our open microcavity (described in ref. 33), we isolate and selectively couple an NV $^-$ to the cavity optical modes. Under non-resonant continuous-wave excitation with a 532 nm wavelength laser, a weak background originating from the diamond unveils the cavity modes (Fig. 1b, color scale capped at 150 cts/s). At regular displacement intervals corresponding to the free-spectral range, the cavity frequency matches an NV $^-$ ZPL transition (dashed and solid squares in Fig. 1b). For all following experiments, we set the cavity length around values corresponding to mode 16, indicated by the solid square in Fig. 1b. A finer scan shows a strong increase in photoluminescence (PL) when resonance conditions are met, and reveals a doublet of peaks, degenerate in emission frequency (Fig. 1c). The doublet originates from the 34.4 GHz-splitting of the cavity's fundamental transverse mode into two orthogonal, linearly polarized modes (M1 and M2, with M2 chosen as the reference mode, i.e. $\Delta_{\rm cav}=0$). Changes in the mode splitting along the membrane and a

significant reduction of the mode splitting out of the membrane hint at birefringence induced by the bonded diamond^{34–36}. The estimated corresponding anisotropic stress value (~65–75 MPa) in the membrane, while not unrealistic, suggests rather a simultaneous straining of the diamond and the DBR, giving rise to the observed birefringence^{28,37}. The exact intensity ratio of the M1 and M2 peaks depends on the coupling strength of the NV⁻ to either mode, combined with the alignment of the polarization-filtered detection channel (see polarization-resolved data in Supplementary Material). From measurements shown in Fig. 1b, we infer that the cavity operates in a mode close to the air-confined condition, a configuration less sensitive to surface scattering losses¹⁶. The measured finesse \mathscr{F} is 4330, corresponding to a quality factor of 42,930 and a decay rate $\kappa = 2\pi \cdot 11.0$ GHz.

We verify that the detected photons stem from a single NV⁻ by performing photon autocorrelation measurements ($g^{(2)}(\tau)$). With the NV⁻ onresonance with mode M1, we correlate the arrival times of the PL photons on two avalanche photodetectors (APDs). The result, normalized to the value at long delay times (33 µs), is shown in Fig. 1d. A pronounced antibunching dip of $g^{(2)}(0) = 0.04 \ll 0.5$ is the clear identifier of a single-photon emitter. The very small $g^{(2)}(0)$ value, considering non-resonant excitation, is a signature of the effect of the cavity: the incoherent background is filtered out.

The $g^{(2)}(\tau)$ data is fitted using a three-level rate-equation model. The choice is justified as the NV⁻ i) is pumped non-resonantly and ii) polarizes into $m_s = 0$, reducing the complexity of the excited state. The inset of Fig. 1d shows the effective states of the model: the NV- ground and excited states $(m_s = 0)$ and the shelving state, including all possible population-trapping mechanisms. The fit closely follows the data and yields the emission, excitation, shelving, and de-shelving rates, respectively: $\{k_{eg}, k_{532}, k_{s}, k_{d}\} = \{101.2,$ 2.5, 32.0, 3.8} MHz. The model interprets the bunching behavior at delays larger than zero, explained by the partial shelving of the population into states not participating in the emission process, typically either the NVsinglet state, the ionized, neutral NV state (NV⁰), or a combination of both. We estimate an NV "on-off" ratio, translatable into an occupation of the triplet states, of ~83%, matching typical values for non-resonantly driven NV^{-5} . Strikingly, k_{eg} the rate representing the spontaneous emission, is noticeably higher than expected for an NV $^-$ polarized in m_s = 0 (101.2 MHz versus ~81 MHz)⁴.

The key physical principle behind this work, the Purcell effect results in a shortened radiative lifetime for an emitter that couples to a resonant optical mode. In fact, the high $k_{\rm eg}$ rate is the first quantifiable manifestation of an acceleration of the NV⁻ dynamics by the cavity (in this case, by mode M1 by a factor ~1.24). Following, we characterize the Purcell-enhancement in our system by exciting the NV⁻ non-resonantly with short pulses of 532 nm light (~70 ps) and monitoring the arrival time of PL photons. The non-resonant pulses guarantee that the NV remains in the NV⁻ charge state

and is m_s = 0 polarized. The radiative lifetime for any particular value of $\Delta_{\rm cav}$ is extracted by fitting the decay signal with a single exponential, taking a common instrument-related rise-time into account.

With the measurement apparatus adjusted such that the polarization of the detection channel and mode M2 coincide, the cavity is swept across $\Delta_{cav}=0$. The PL signal rate Π at delay time $\tau=0$ follows a Lorentzian distribution centered at $\Delta_{cav}=0$ with a full-width half-maximum (FWHM) of 80 pm (Fig. 2a). The lifetimes on the other hand, show not one, but two dips (Fig. 2b). While the dip at $\Delta_{cav}=0$, corresponding to the resonance condition with mode M2, is the most pronounced, another clear lifetime reduction dip can be see around $\Delta_{cav}=-210$ pm, corresponding to the resonance condition with mode M1. The coupling between the NV $^-$ and M1 opens an additional decay channel, which can be observed in the decay dynamics, despite not directly detecting photons leaking from mode M1. For positive cavity displacements Δ_{cav} , the extracted lifetimes tend toward the original, uncoupled value $\tau_0=1/\gamma_0$. Note that the decrease in signal strength at such detunings leads to an increased uncertainty (shaded gray bars).

Interestingly, the lifetime reduction dip and the corresponding signal peak around $\Delta_{\rm cav}=0$ exhibit noticeably different widths (116 pm versus 80 pm FWHM). The broader features in the lifetime reduction are well explained by taking into account residual relative motion $\sigma_{\rm vib}$ between the mirrors (mechanical noise). We derive a model parametrized by the coupling of both cavity modes to a single, linearly polarized NV⁻ transition and by the residual mechanical vibration level $\sigma_{\rm vib}$, and fit it to the entire dataset. The model closely reproduces the features of the data and provides insight into the observed broadening of the lifetime dips (light blue line in Fig. 2).

Vibrations add noise to the detuning between the cavity modes and the NV $^-$ transition. As reduced detuning leads to both faster decay and higher signal, "early photons" are over-represented, and the extracted lifetimes appear shorter. The deviations between the model and the data around mode M1 are likely due to a temporary increase in background mechanical noise. The fit further provides a value for the angle of the projection of the optical dipole moment with respect to mode M2: $\theta_{\rm cav}=33(4)^{\rm o},~\sigma_{\rm vib}=22.0(1)~\rm pm^{\rm cms},~and~the~vibration-free~Purcell~factors~for~M1~and~M2:~1.44(9)~and~2.068(5). Finally, we can evaluate the NV<math display="inline">^-$ lifetime unmodified by the cavity, yielding $\tau_0=12.35(4)~\rm ns,~in~excellent~agreement~with~previously~reported~NV<math display="inline">^-$ excited-state lifetimes in bulk diamond $^{4.39,40}$.

Figure 2c shows decay traces for three specific cavity detunings: on resonance with cavity mode M1, on resonance with cavity mode M2, and far off-resonance with either mode. The extracted lifetimes are 10.6(6) ns for mode M1 and 6.88(4) ns for mode M2. It is worth noting the consistency between the lifetime measured at resonance with mode M1 and the inverse rate $1/k_{eg}$ extracted from the $g^{(2)(\tau)}$ data (9.9(7) ns). For the far-off resonance trace, the lifetime is found to be 12.3(2) ns, in agreement with the previously mentioned value of τ_0 . The vibration-limited lifetimes for M1 and M2, together with τ_0 , are used for all following calculations.

Denoting the NV $^-$ total, cavity-modified, decay rate as y_P , the overall Purcell-enhancement can be expressed as

$$F_{\rm P} = \gamma_{\rm P}/\gamma_0 = 1 + \frac{4g_{\rm ZPL}^2}{\kappa \gamma_0}.$$

This definition explicitly includes the emission into the incoherent PSB and the free-space continuum. We extract an overall Purcell-factor of $F_{\rm P,M1}$ = 1.15(6) and $F_{\rm P,M2}$ = 1.79(1) for mode M1 and mode M2, respectively. With the probability of spontaneous emission into the cavity mode defined as β = $(F_{\rm P}-1)/F_{\rm P}$, we retrieve $\beta_{\rm M1}$ = 13(5)% and $\beta_{\rm M2}$ = 44.1(6)%.

Since only a fraction of the total NV^- emission—the ZPL— is enhanced by the cavity, a small overall Purcell factor conceals a significant Purcell-enhancement of the ZPL alone, which can be described by

$$F_{\rm P}^{ZPL} = \frac{F_{\rm P} - (1 - \xi_0)}{\xi_0}$$

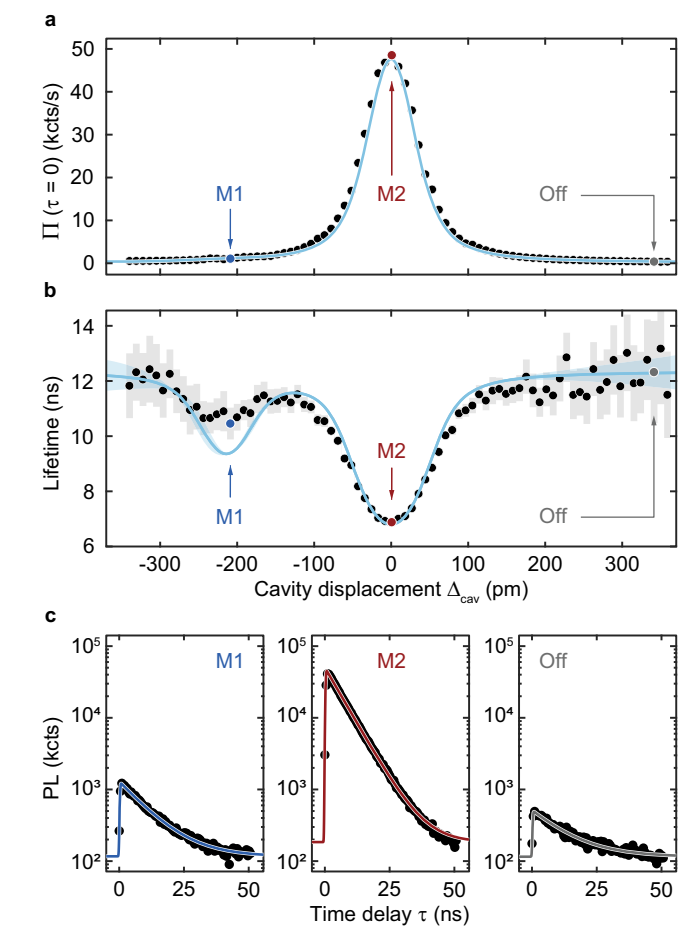


Fig. 2 | Mode-selective Purcell-enhancement under pulsed non-resonant excitation. a ZPL emission rate at zero-delay (full black circles) for a collection path copolarized with mode M2. b Extracted single-exponential decay times (full circles). The coupling of the NV⁻ to either cavity mode yields a lifetime reduction at the respective cavity displacement values. The fit in panels a and b (light blue line) accounts for both modes as well as for residual cavity vibrations. Shaded areas represent 95% confidence intervals on fits and 1.96 standard deviations on data points. c ZPL temporal decays for cavity displacement values corresponding to mode M1 (navy), mode M2 (burgundy), and off-resonance with either mode (gray).

with ξ_0 denoting the Debye-Waller factor, here taken as $3\%^{14}$. We obtain a ZPL Purcell-factor of $F_{\rm P,M1}^{ZPL}=6.0(3)$ and $F_{\rm P,M2}^{ZPL}=27.3(3)$ for mode M1 and mode M2, respectively.

Alternatively, the effect of the cavity can be seen as modifying the Debye-Waller factor, dramatically increasing the coherent emission probability. The cavity-enhanced Debye-Waller factor can be written as

$$\xi_{\rm cav} = \beta + \frac{\xi_0}{F_{
m p}} \approx \beta.$$

Following, when mode M2 is tuned into resonance with the NV $^-$, the branching ratio between ZPL and PSB emission is increased by more than an order of magnitude. In other words, almost half of the NV $^-$ coherent emission ($\xi_{\rm cav} \sim \beta_{\rm M2} = 44.1(6)\%$), normally spoiled by phonons in the bulk, is restored

An estimate of the NV⁻-cavity coupling strength can be extracted from $F_{P,M2}$, completing the set of cavity quantum electrodynamics parameters $\{g_{ZPL}, \kappa, \gamma_0\} = 2\pi \cdot \{167(19), 1.1 \cdot 10^4, 12.89(4)\}$ MHz. Here, we assume that γ_0 is given purely by the emitter decay rate off-resonance with the cavity. This

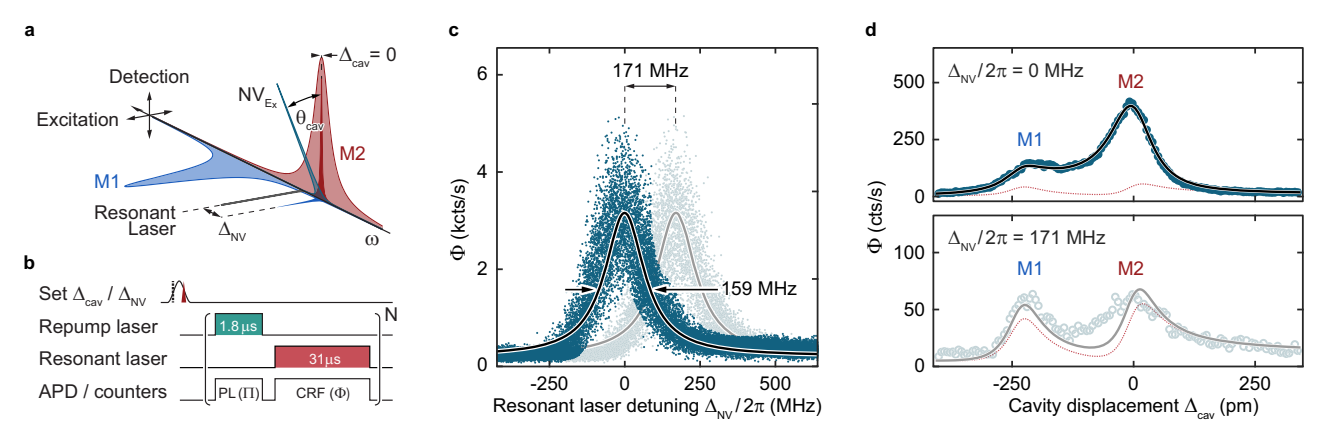


Fig. 3 | NV⁻ resonance fluorescence. a For all CRF measurements, the cross-polarized excitation and detection channels are co-polarized with modes M1 (navy) and M2 (burgundy), respectively. Mode M2 is depicted as on-resonance with the NV⁻ E_x ZPL transition (teal). Spectral overlap between the modes and the projection of the E_x dipole moment on both modes enable resonant excitation (resonant laser, gray peak) via mode M1 and CRF collection via mode M2. **b** Pulse sequence for CRF measurements. ZPL photons are sorted as PL (emitted during the repump pulse at rate Π) or CRF (emitted during the resonant pulse at rate Φ). **c** Resonant laser frequency sweep (1 nW) through the coupled transition for $\Delta_{\text{cav}} = 0$. The teal and blue-gray resonances correspond to the same E_x transition (linewidth 159 MHz),

Stark-shifted (by 171 MHz) by a single charge trapped in the vicinity of the NV⁻. Zero laser detuning corresponds to a frequency of 469.7 THz. **d** Sweep of the cavity length, changing the laser-M1 detuning together with the detuning between E_x and both modes. The laser power is lowered with respect to **c** (0.1 nW) to highlight the difference in response between the case at $\Delta_{\rm NV}=0$ (top) and $\Delta_{\rm NV}/2\pi=171$ MHz (bottom). The change in amplitude ratio between the M1 and M2 peaks is the signature of non-linearity in the response of the NV⁻. The model describing both data sets includes two modes coupling to a single saturable transition (black and gray lines) and includes the laser background (dashed red lines).

approximation neglects dephasing effects, yielding a lower bound. A justification to this simplification is that at low enough temperature and provided that the NV⁻ transitions are driven strictly resonantly, Fourier-transformed linewidths are achievable¹⁰. The obtained values, with $\kappa \gg g_{ZPL} \gg \gamma_0$, place the interaction in the weak coupling (fast cavity) regime, but also at the onset of the high-cooperativity regime ($C = F_P - 1 > 1$), for which interactions between the cavity field and the emitter become significant at the single-photon level.

Cavity-assisted resonance fluorescence

A cornerstone of quantum optics is the ability to coherently and resonantly drive a given optical transition. For NV⁻ centers, this ability lies at the heart of resonant spin read-out⁶ and spin-photon entanglement generation^{7,8}. A sizeable challenge is to filter the resonantly scattered photons (the resonance fluorescence) from the driving laser photons. We obtain laser extinction ratios of ~50 dB by aligning the excitation and detection channels with modes M1 and M2, as illustrated in Fig. 3a. The respective projections of the NV⁻ dipole moment on modes M1 and M2 allow us to drive the transition (in this case the cycling $m_s = 0 \leftrightarrow E_x$ transition, referred to as E_x , see Supplementary Material) via mode M1, while detecting CRF via the preferentially coupled mode M2. This configuration is kept for all the following experiments. Once again, the cavity plays a crucial role in amplifying (i) the resonance fluorescence signal and (ii) the intra-cavity power, enabling us to measure CRF with high SLR.

The NV⁻ is excited using interleaved non-resonant "repump" (532 nm, 1.8 μ s, 200 μ W if not specified otherwise) and resonant (637 nm, 31 μ s) pulses separated by 400 ns (Fig. 3b). The detected photons are either binned or tagged according to their time of arrival, allowing the identification and monitoring of PL and CRF signals. The repump pulses are primarily used to convert NV⁰ to NV⁻ and to restore the $m_s = 0$ population after shelving into $m_s = \pm 1$ by the resonant pulses, but we also use the light generated during this interval to measure PL and conduct periodical checks on the cavity displacement, ensuring drift-free operation.

Maintaining the condition $\Delta_{\rm cav}=0$ and sweeping the resonant laser detuning $\Delta_{\rm NV}$ (center frequency $\nu_{\rm NV}=469.7$ THz), we realize a first unambiguous measurement of CRF from a Purcell-enhanced NV $^-$ (Fig. 3c). Two peaks (teal and blue-gray) can be distinguished, both corresponding to $E_{\rm x}$ and extrinsically broadened by charge noise generated by the high-energy repump pulses. The doublet is a striking manifestation of resolved charge

noise: during a repump pulse, a nearby trap state stochastically captures or releases an electron, leading to different Stark fields and the emergence of two distinct center frequencies for $E_{\rm x}$ (see Methods and Supplementary Material). The observation of single-trap loading and unloading highlights the quality of the diamond material and of the NV centers formed via carbon implantation post-fabrication³². Sub-hertz trap dynamics make the post-selection (based on CRF intensity) between the two trap configuration straightforward. The 171(3) MHz blue-shifted state is then only used to evaluate the effect of a fixed detuning.

The extrinsic broadening of E_x is best fitted by a model taking into account the expected Purcell-induced increase of the homogeneous linewidth. As confirmed later, the resonant laser power used in this measurement (1 nW) allows us to neglect power broadening and extract a Lorentzian-distributed linewidth with a FWHM $\Gamma_{ext}/2\pi$ = 159(5) MHz. This value agrees well with previously measured samples created with the same method³² and is instrumental in enabling the measurement of CRF. A broader linewidth (typically > 1 GHz), common for microfabricated structures, would result in i) a significant spread of Δ_{cav} , the pulse-to-pulse detuning between the transition and the cavity ($\kappa/2\pi = 11$ GHz), effectively reducing the Purcell factor and ii) a decreased average resonant driving efficiency, leading to a vanishing SLR and precluding CRF measurements. In the case presented in Fig. 3c, the fit yields a SLR of 14.0, corresponding to a contrast of 93.3%. To our knowledge, it constitutes the only report so far of resonance fluorescence from an NV measured with a SLR exceeding 1 without relying on temporal filtering^{19,41,42}.

CRF as a function of cavity displacement is shown in Fig. 3d. The top panel represents the condition $\Delta_{\rm NV}=0$. For $\Delta_{\rm cav}=0$, both the laser and mode M2 are on-resonance with $E_{\rm x}$. For moderate cavity displacement, the driving field is approximately constant since the laser only interacts with the cavity via mode M1. Thus, for small values of $\Delta_{\rm cav}$, only the coupling strength between $E_{\rm x}$ and mode M2 varies, leading to the observation of a strong CRF peak. As the cavity displacement is further increased in the negative direction, a second peak emerges, corresponding to the laser being resonantly enhanced by mode M1. The drive enhancement increases the excited state population but simultaneously promotes non-cycling mechanisms such as spin-flips and ionization. Concomitantly, the coupling between $E_{\rm x}$ and M2, the collection mode, is reduced, resulting in a drop in CRF signal and a decrease of the Purcell enhancement. A combination of these effects explains the difference in prominence between the peaks

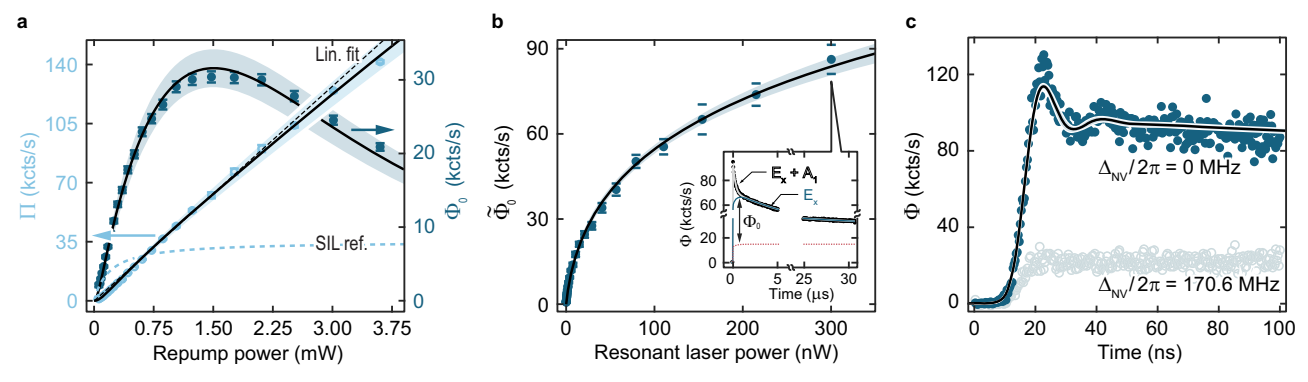


Fig. 4 | **Cavity-enhanced zero-phonon emission.** a ZPL PL (end of the repump pulse, empty light blue circles, left ordinate) and CRF (full teal circles, right ordinate) rates as a function of repump power. The data sets are jointly fitted with a rate-equation model (solid black lines). Deviations from linear best fit (dashed black line) are visible at low and high power. An example of state-of-the-art ZPL count rates for an NV $^-$ in a SIL, extracted from ref. 41, is shown as a light blue, dashed line (left ordinate). **b** CRF rates as a function of resonant laser power. The rates correspond to the nominal amplitude of the $E_{\rm x}$ signal, corrected for laser background and decreasing repump efficiency(details in Supplementary Material). The data are fitted

with a steady-state two-level saturation model, including extrinsic broadening (black line). Inset: Slow CRF decay (300 nW, 30 ns bin-time). The total signal (solid gray line) includes E_x fluorescence (teal line) as well as near-resonant fluorescence from the A_1 state and laser background (red dashed line). c CRF at small time delays (300 nW, 300 ps bin-time). For $\Delta_{\rm NV}=0$ (full teal circles), the signal oscillations are well-captured by a model based on a driven two-level system (black line). A control experiment (blue-gray open circles) with $\Delta_{\rm NV}/2\pi=171$ MHz shows no oscillations (washed out by charge noise and rise-time). On all graphs, shaded intervals (error bars) correspond to a 95% confidence interval (1.96 standard deviations).

associated with modes M1 and M2: for a large-enough laser power, the signal gain obtained due to a stronger drive does not compensate the reduction induced by the cavity displacement.

The bottom panel of Fig. 3d shows the effect of introducing detuning in the same experiment ($\Delta_{\rm NV}=2\pi\cdot 171$ MHz, induced by the charge trap and thus measured in the same experimental run). The detuning effectively results in a reduction of the excited state population for otherwise identical parameters. Since the laser power is unchanged, the SLR decreases. However, the difference between the M1 and M2 peak heights vanishes, indicating that for this effective driving power, the response is linear: the loss of signal due to the cavity displacement is compensated by an increase in driving strength. The data shown in Fig. 3d are well-reproduced by taking into account two modes coupled with different $g_{\rm ZPL}$ values to one saturable transition subjected to charge noise. Using the experimentally-determined values for γ_0 , $\Gamma_{\rm ext}$, $F_{\rm P,M1}$, $F_{\rm P,M2}$ and the laser background, we reduce the free parameters to two scaling factors, one for the collected signal and one for the input power.

We turn our attention toward the evolution of PL and CRF rates as a function of the repump laser power. The NV $^-$ is excited using the same sequence as depicted in Fig. 3b, with the laser, cavity, and $E_{\rm x}$ transition on resonance ($\Delta_{\rm cav}=\Delta_{\rm NV}=0$). The resonant "probe" pulse is kept at a constant power of 5 nW. The PL signal Π (collected during the repump pulses) is shown in Fig. 4a (empty light blue circles, left ordinate). The increase in Π deviates in a subtle way from a linear behavior at high power. The maximal count rate measured amounts to 140.0 kcts/s, limited by the power density available to excite the NV. We stress that the photons collected here are exclusively ZPL photons, and reference our results against the ZPL intensities obtained for state-of-the-art measurements using an NV $^-$ embedded in a SIL, coated optics, and active aberration correction (dashed light blue line, left ordinate, reproduced from ref. 41). The still unsaturated count rate measured with the cavity already exceeds the SIL performance by a factor four.

The effect of increased repump power can also be seen in the CRF signal (Fig. 4a, full teal circles, right ordinate). Since the resonant power is kept constant, the early CRF signal Φ_0 (before spin-shelving or ionization takes place, i.e., for times less than ~1 µs) is directly proportional to the pulse-averaged joint probability of the NV to be in the correct charge (NV $^-$) and spin ($m_{\rm s}=0$) state. The linear increase of the Φ_0 for repump powers below 1.5 mW thus indicates an improvement in the NV $^-$ initialization. Combining this observation with the roughly linear increase in Π , whose intensity depends mostly on the product of the repump power and the NV $^-$ population, hints at a quicker recovery of the maximal charge population

compared to its spin counterpart. The decrease in Φ_0 beyond 1.5 mW results from an optically-induced drift of E_x in frequency, leading to $\Delta_{\rm NV} \neq 0$ and a consequentially reduced signal (see Fig. S3e, f in Supplementary Material).

The Π and Φ_0 signals are jointly fitted (solid black curves) using two coupled models: a 10-state model for the NV optical cycle under non-resonant excitation⁴³, and an effective 3-state model describing the population evolution during the resonant pulse (see Fig. S3 in Supplementary Material for details). The joint fit allows for a more robust retrieval of estimates for the PL saturated count rate $\Pi_{\rm sat}$ and saturation power $P_{\rm nr,sat}$. The regression yields $P_{\rm nr,sat}=67(37)$ mW, far from the maximal power experimentally available (3.6 mW), a clear evidence for the low power density in our experiment. The estimated saturated count rate $\Pi_{\rm sat}$ of 2.3(6) Mcts/s is consistent with a cavity-enhanced $\xi_{\rm cav,M2}=0.45$ and $F_{\rm P,M2}=1.8$: the cavity bandwidth restricts collection to ZPL photons, but the muchimproved branching ratio and radiative rate compensate for the undetected PSB. Overcoming the engineering challenges limiting the non-resonant power density would lead to detection rates on-par with the best non-resonant photonic structures, despite recording only ZPL photons 12,41,44 .

In Fig. 4b, we increase the resonant laser power and extract $\tilde{\Phi}_0$, the E_x transition CRF intensity before shelving. In order to prevent power-induced drifts and potential degradation of the sample, the repump power is kept at 0.2 mW. Due to a combination of strain, charge noise, and incomplete initialization, the close-by A_1 transition is also weakly driven for the highest resonant powers. The E_x fraction of the signal is recovered from the total signal by fitting its bi-exponential decay: when excited to the A_1 state, the NV⁻ is prone to undergo inter-system crossing (ISC), leading to a characteristic fast relaxation 45,46 (see inset). Further, for each measurement point, the residual laser background is subtracted and the $\tilde{\Phi}_0$ signal is rescaled by the ratio between the measured Π rate over the Π at lowest resonant power. The latter step partially corrects for incomplete spin and charge initialization. For details on laser background determination and PL normalization, see ref.

For the highest resonant power available, the $\tilde{\Phi}_0$ intensity reaches 86 kcts/s. The saturation behavior is modeled by convolving the steady-state response of a resonantly driven two-level system with the previously measured Lorentzian broadening:

$$\tilde{\Phi}_0 = \Phi_{\text{sat}} \frac{2aP_{\text{res}}}{2aP_{\text{res}} + F_{\text{P,M2}}^2 \gamma_0^2 + 2\Gamma_{\text{ext}} \sqrt{2aP_{\text{res}} + \gamma_0^2 F_{\text{P,M2}}^2}}.$$
 (1)

Here, the quickly decaying coherent response and the shelving processes have been disregarded, owing to the coarse time-binning and slow shelving. A scaling constant for the power ($a=1.7(5)\cdot 10^3$ MHz²/nW, accounting for all optical losses and coupling efficiencies) and the saturated rate ($\Phi_{\rm sat}$) are left as the only free parameters. $\Phi_{\rm sat}$ amounts to 250(30) kcts/s, underlining once more the ability of the coupled NV⁻-cavity system to outmatch traditional photonic structures. The associated saturation power $P_{\rm res,sat}=1.2(1)~\mu{\rm W}$ (corresponding to half the saturated intensity) is predictably large as it would correspond to a Rabi frequency sufficient to overcome the charge noise-induced detuning distribution.

Finally, in Fig. 4c, we examine the time evolution of the CRF signal while driving the NV⁻ with the highest resonant power available (300 nW). For $\Delta_{NV} = 0$, coherent effects in the form of Rabi oscillations can be resolved. The oscillation contrast is reduced by residual laser background and A₁ transition fluorescence (~60% of total signal), while charge noise and a slow pulse rise-time (9.5 ns, see ref.) contribute to a smearing of the oscillatory response. Taking into account these factors and considering the cycling character of the E_x transition, we reproduce the data with a model based on the optical Bloch equations. The result of the fit, shown as a solid black line, yields the zero-detuning Rabi frequency $\Omega_{R.0}/2\pi = 51.1(26)$ MHz. A control experiment is done for a drive detuning of $\Delta_{NV}/2\pi = 171$ MHz. The fast oscillations for a detuned Rabi drive $\Omega_{R,171}$ are expected to be filtered out by the slow rise-time and charge noise, a prediction confirmed by our data: the smooth response rules out any artifacts stemming from the driving pulse shape in the zero-detuning dataset. The results in Fig. 4c demonstrate that the cavity-coupled E_x transition can be driven coherently, opening opportunities for near-unity excitation probability using fast π pulses.

Discussion

Comparing the extracted Rabi frequency on resonance $\Omega_{R,0} \sim 2.2 \cdot \gamma_0 F_{P,M2}$ to the expected (based on the data fitted to Eq. (1)) Rabi frequency at 300 nW, $\Omega_{R,0}^{exp} \sim 5 \cdot \gamma_0 F_{P,M2}$ indicates that the non-linear behavior observed in Fig. 4b is not entirely due to two-level saturation. The premature saturation of E_x is instead likely to be caused by a reduction in initial $m_s = 0$ population as the resonant power is increased (see Fig. S2 in Supplementary Material), explaining the difference between Φ_{sat} and I_{sat}^{PL} . While increasing the repump power improves the NV- initialization, non-resonant spinpumping might be less efficient with the cavity on-resonance with the NV upper orbital branch: the only state for which the spin-conserving decay probability increases significantly is A_1 , with spin-projection $m_s = \pm 1$ implying a slower polarization rate into $m_s = 0$. A more favorable path forward is enabled by the observation of the A1 transition (see Supplementary Material) and would exploit resonant spin-pumping to achieve high-fidelity initialization⁶. Spin population initialization and control would limit the use of the green repump pulse to charge-state initialization. Implemented as previously demonstrated "charge-resonance (CR) checks" techniques¹⁰, it would enable charge-noise-free operation. This would in turn lead to the generation of lifetime-limited photons and an automatic increase of the SLR by a factor $\sim \frac{\Gamma_{\rm ext}}{\gamma_0 F_{\rm p}} = 6.9$, bringing it from our measured value of 14.0 (from Fig. 3) to ~100, closer to the value needed to perform high-fidelity readout or spin-photon entanglement. We note that a reduced mode splitting would also have an important impact on the SLR, as the ratio of intra-cavity over propagating power would increase.

The results presented in this study were obtained at a location where diamond-induced losses limit the finesse to 4 330 (for a bare-cavity finesse of $\mathcal{F}_{bare}=8\,880$), impacting the Purcell factor, β -factor, and ultimately the excitation-to-photon cavity outcoupling efficiency

$$\eta = \beta \frac{\kappa_{top}}{\kappa + \gamma_0}.$$

Here, κ_{top} is the decay rate out of the top mirror. For our measured parameters, $\eta_{M2}=14.8\%$. The outcoupling efficiency could still be increased, considering the highest finesse $\mathcal{F}=6\,700$ recorded on the same membrane (corresponding to a loss rate comparable to ref. 23, albeit for an air-like mode). Operation at such a finesse would bring the Purcell factor to $F_P=2.2$

and the efficiency to $\eta=28\%$. The limit to our collection efficiency (~10%), while set in part by the silicon APDs (~70%), stems mostly from the optics in the path, in particular by the objective transmission (~45%) and aberrations. More mature implementations with quantum dots present an optimistic perspective^{24,47}, bringing the realization of a total (end-to-end) efficiency Σ ~ 15% within reach, and consequently a tremendous improvement over current NV⁻-based spin-photon interfaces.

In conclusion, we have demonstrated an efficient photonic interface to an isolated, narrow-linewidth NV center, a spin-based qubit in diamond with a proven track-record. With Purcell factors of up to 1.79, the interaction of the NV⁻ with light is profoundly altered, and the coherent emission fraction is increased by more than an order of magnitude, from 3% to 44.7%. This allows us to measure ZPL count rates exceeding 140 kcts/s under non-resonant excitation and resonance fluorescence count rates reaching 86 kcts/s with a signal-to-laser ratio largely exceeding unity, without any temporal filtering. Our work represents crucial progress in addressing a problem that has, until now, stymied the development of prototypical quantum networks and limited their extension beyond a few nodes^{9,31}. Projecting the current system efficiency to spin-spin entanglement rates, our system could already increase the success probability of one (two) photon protocols by more than one (two) order of magnitudes $9,\overline{3}1,41,48$, opening opportunities for the implementation of the NV--cavity platform as an efficient building block for quantum networks49-51

Methods

Cavity and sample

The top mirror curvature is created via CO_2 laser ablation following a previously developed method 33,52 . Aberrations in the ablating laser beam lead to a slight ellipticity (typically ~5%) of the crater. The top (bottom) DBR mirror transmission amounts to $\mathcal{F}_{top}=485$ ppm ($\mathcal{F}_{bottom}=56$ ppm). Both mirrors are high-index terminated, with a stopband centered around 637 nm and <30% reflective at 532 nm. The additional scattering and absorption losses at the measurement site amount to $\mathcal{L}=908.7$ ppm.

NV centers are created in 20-by-20 μm^2 membranes by implantation post-fabrication as described in ref. 32. The ions ($^{12}C^+$) are implanted with an energy of 50 keV and a fluence of 5 \cdot 10 8 cm $^{-2}$, aiming at forming sparse NVs at a depth of ~66 nm, close to a field antinode in a subsequently assembled cavity. Membranes are released by micromanipulators onto a bottom mirror, where they are bonded via van der Waals interactions to the mirror's surface (implanted side against the mirror). The bottom mirror is mounted on a set of XYZ piezosteppers (attocube ANP51). The top mirror is bolted onto a surrounding frame and adjusted in order to achieve mirror parallelity <0.4 mrad 20 . The full cavity is supported by another set of XYZ steppers (attocube ANP101), placed in a housing under a fixed three-lens objective and suspended in a tube filled with 20–30 mbar of high-purity helium. The entire tube is cooled in a super-insulated helium-bath cryostat to ~4 K.

Setup

The sample is illuminated non-resonantly either by a low-coherence laser at 532 nm (continous-wave and resonance fluorescence experiments) or the 5 nm-filtered output of a pulsed (\sim 70 ps) supercontinuum laser (NKT Photonics SuperK, lifetime experiments). Resonant excitation is done with a narrow-linewidth external-cavity diode laser (Toptica DLPro) locked to a wavemeter. Both CW lasers are intensity-gated by AOMs (Gooch & Housego) in a double-pass configuration, providing an isolation of >60 dB. The collected fluorescence is long-pass-filtered (\sim 594 nm), optionally bandpass-filtered (\sim 636 \pm 4 nm, Semrock), coupled to a fiber, and detected using either one APD, a pair of APDs (Excelitas SPCM-AQRH), or a diffraction grating spectrometer and liquid nitrogen-cooled back-illuminated CCD (Princeton Instruments Acton 2500i and Pylon camera). The signal from the APDs is recorded either in a histogram or time-tagged mode by a timing module (Picoquant Picoharp 300). The triggers for the timing module and AOM pulsing are sent by a dual-output function generator

(Agilent 33500B). All DC voltages are generated by a 24-bit digital-to-analog card (Basel Precision Instruments), amplified if needed by low-noise 10x amplifiers (Electronics workshop, University of Basel).

PL and CRF measurements

The spectra in the scans presented in Fig. 1 are recorded with integration times 1-3 s at a non-resonant power of ~1 mW. The high-resolution scan is dispersed using a high-density (2160 grooves/mm) grating, resulting in a slightly asymmetric peak. The autocorrelation signal is recorded using a Hanbury Brown-Twiss setup for a duration of 20 min at a non-resonant power of ~1.9 mW. An automatic "relock" protocol corrects for drifts in Δ_{cav} every 5 min. Each decay trace as a function of Δ_{cay} in Fig. 2 is integrated for 90 s, with a cavity "relock" every 5 min. The CRF scans in Fig. 3c and d are averaged from sets of 50 and 70 scans, respectively, recorded with 0.1 s integration time per point. During each scan, the nearby trap can become loaded or unloaded. histogramming the counts for each (Δ_V or Δ_{cav}) setpoint yields a bi-modal distribution, allowing the attribution of each of the scan setpoints to either the "loaded" or "unloaded" state. The data sets used in Fig. 4 are acquired by time-tagging the start of each non-resonant pulse on one channel of the timing module and the arrival of all photons on another channel. The integration time for each power setpoint is 10 min, after which a "relock" sequence is run. The time-tagged data can then be recast as average intensities per pulse (allowing discrimination of the trap state), or as averaged time-traces.

Data availability

The data that support the findings of this study are available from the corresponding authors upon reasonable request.

Code availability

The code that has been used to analyze the data is available from the corresponding authors upon reasonable request.

Received: 15 May 2024; Accepted: 27 October 2024; Published online: 07 November 2024

References

- Bar-Gill, N., Pham, L. M., Jarmola, A., Budker, D. & Walsworth, R. L. Solid-state electronic spin coherence time approaching one second. *Nat. Commun.* 4, 1743 (2013).
- Maurer, P. C. et al. Room-temperature quantum bit memory exceeding one second. Science 336, 1283–1286 (2012).
- Abobeih, M. H. et al. One-second coherence for a single electron spin coupled to a multi-qubit nuclear-spin environment. *Nat. Commun.* 9, 2552 (2018).
- Robledo, L., Bernien, H., Sar, T. V. D. & Hanson, R. Spin dynamics in the optical cycle of single nitrogen-vacancy centres in diamond. *N. J. Phys.* 13, 025013 (2011).
- Doherty, M. W. et al. The nitrogen-vacancy colour centre in diamond. Phys. Rep. 528, 1–45 (2013).
- Robledo, L. et al. High-fidelity projective read-out of a solid-state spin quantum register. *Nature* 477, 574–578 (2011).
- 7. Togan, E. et al. Quantum entanglement between an optical photon and a solid-state spin qubit. *Nature* **466**, 730–734 (2010).
- Bernien, H. et al. Heralded entanglement between solid-state qubits separated by three metres. *Nature* 497, 86–90 (2013).
- 9. Pompili, M. et al. Realization of a multinode quantum network of remote solid-state qubits. *Science* **372**, 259–264 (2021).
- Hermans, S., Martins, L. D. S., Montblanch, A. R. & Beukers, H. Entangling remote qubits using the single-photon protocol: an indepth theoretical and experimental study. *N. J. Phys.* 25, 013011 (2023).
- Jamali, M. et al. Microscopic diamond solid-immersion-lenses fabricated around single defect centers by focused ion beam milling. Rev. Sci. Instrum. 85, 123703 (2014).

- Hadden, J. P. et al. Strongly enhanced photon collection from diamond defect centers under microfabricated integrated solid immersion lenses. *Appl. Phys. Lett.* 97, 241901 (2010).
- Barclay, P. E., Fu, K.-M., Santori, C. & Beausoleil, R. G. Hybrid photonic crystal cavity and waveguide for coupling to diamond NVcenters. Opt. Express 17, 9588–9601 (2009).
- Faraon, A., Santori, C., Huang, Z., Acosta, V. M. & Beausoleil, R. G. Coupling of nitrogen-vacancy centers to photonic crystal cavities in monocrystalline diamond. *Phys. Rev. Lett.* **109**, 033604 (2012).
- 15. Li, L. et al. Coherent spin control of a nanocavity-enhanced qubit in diamond. *Nat. Commun.* **6**, 6173 (2015).
- Janitz, E. et al. Fabry-Perot microcavity for diamond-based photonics. *Phys. Rev. A* 92, 1–11 (2015).
- Johnson, S. et al. Tunable cavity coupling of the zero phonon line of a nitrogen-vacancy defect in diamond. N. J. Phys. 17, 122003 (2015).
- Riedel, D. et al. Deterministic enhancement of coherent photon generation from a nitrogen-vacancy center in ultrapure diamond. *Phys. Rev. X* 7, 031040 (2017).
- Ruf, M., Weaver, M. J., Van Dam, S. B. & Hanson, R. Resonant excitation and Purcell enhancement of coherent nitrogen-vacancy centers coupled to a fabry-perot microcavity. *Phys. Rev. Appl.* 15, 024049 (2021).
- Barbour, R. J. et al. A tunable microcavity. J. Appl. Phys. 110, 053107 (2011).
- Albrecht, R., Bommer, A., Deutsch, C., Reichel, J. & Becher, C. Coupling of a single nitrogen-vacancy center in diamond to a fiber-based microcavity. *Phys. Rev. Lett.* 110, 243602 (2013).
- 22. Wang, D. et al. Turning a molecule into a coherent two-level quantum system. *Nat. Phys.* **15**, 483–489 (2019).
- Høy Jensen, R. et al. Cavity-enhanced photon emission from a single germanium-vacancy center in a diamond membrane. *Phys. Rev. Appl.* 13, 064016 (2020).
- 24. Tomm, N. et al. A bright and fast source of coherent single photons. *Nat. Nanotechnol.* **16**, 399–403 (2021).
- Flågan, S. et al. A diamond-confined open microcavity featuring a high quality-factor and a small mode-volume. J. Appl. Phys. 131.0 113102 (2022).
- Bayer, G. et al. Optical driving, spin initialization and readout of single siv- centers in a fabry-perot resonator. Commun. Phys. 6, 300 (2023).
- Deshmukh, C. et al. Detection of single ions in a nanoparticle coupled to a fiber cavity. Optica 10, 1339–1344 (2023).
- Zifkin, R., Rodríguez Rosenblueth, C. D., Janitz, E., Fontana, Y. & Childress, L. Lifetime reduction of single germanium-vacancy centers in diamond via a tunable open microcavity. *PRX Quant.* 5, 030308 (2024).
- Herrmann, Y. et al. Coherent coupling of a diamond tin-vacancy center to a tunable open microcavity. https://arxiv.org/abs/2311. 08456 (2023).
- Pallmann, M. et al. Cavity-mediated collective emission from few emitters in a diamond membrane. https://arxiv.org/abs/2311.12723 (2023).
- 31. Hermans, S. L. N. et al. Qubit teleportation between non-neighboring nodes in a quantum network. *Nature* **605**, 1–23 (2021).
- Yurgens, V. et al. Spectrally stable nitrogen-vacancy centers in diamond formed by carbon implantation into thin microstructures. *Appl. Phys. Lett.* 234001, 234001 (2022).
- Greuter, L. et al. A small mode volume tunable microcavity: Development and characterization. *Appl. Phys. Lett.* 105, 121105 (2014).
- 34. Grimsditch, M., Anastassakis, E. & Cardona, M. Piezobirefringence in diamond. *Phys. Rev. B* **19**, 3240 (1979).
- Howell, D. Strain-induced birefringence in natural diamond: a review. Eur. J. Mineral. 24, 575–585 (2012).
- Tomm, N. et al. Tuning the mode splitting of a semiconductor microcavity with uniaxial stress. Phys. Rev. Appl. 15, 054061 (2021).

- Guo, X. et al. Microwave-based quantum control and coherence protection of tin-vacancy spin qubits in a strain-tuned diamondmembrane heterostructure. *Phys. Rev. X* 13, 041037 (2023).
- Purcell, E. M. Spontaneous emission probabilities at radio frequencies. *Phys. Rev.* 69, 681 (1946).
- Batalov, A. et al. Temporal coherence of photons emitted by single nitrogen-vacancy defect centers in diamond using optical rabioscillations. *Phys. Rev. Lett.* 100, 077401 (2008).
- Tamarat, P. et al. Stark shift control of single optical centers in diamond. *Phys. Rev. Lett.* 97, 083002 (2006).
- Hensen, B. et al. Loophole-free Bell inequality violation using electron spins separated by 1.3 kilometres. *Nature* 526, 682–686 (2015).
- Tran, T. H., Siyushev, P., Wrachtrup, J. & Gerhardt, I. Extinction of light and coherent scattering by a single nitrogen-vacancy center in diamond. *Phys. Rev. A* 95, 053831 (2017).
- Happacher, J. et al. Low-temperature photophysics of single nitrogenvacancy centers in diamond. *Phys. Rev. Lett.* 128, 177401 (2022).
- Hedrich, N., Rohner, D., Batzer, M., Maletinsky, P. & Shields, B. J. Parabolic diamond scanning probes for single-spin magnetic field imaging. *Phys. Rev. Appl.* 14, 064007 (2020).
- Goldman, M. L. et al. State-selective intersystem crossing in nitrogenvacancy centers. *Phys. Rev. B* 91, 165201 (2015).
- Goldman, M. L. et al. Phonon-induced population dynamics and intersystem crossing in nitrogen-vacancy centers. *Phys. Rev. Lett.* 114, 145502 (2015).
- Ding, X. et al. High-efficiency single-photon source above the losstolerant threshold for efficient linear optical quantum computing. https://arxiv.org/abs/2311.08347 (2023).
- 48. Barrett, S. D. & Kok, P. Efficient high-fidelity quantum computation using matter qubits and linear optics. *Phys. Rev. A* **71**, 060310 (2005).
- Childress, L., Taylor, J. M., Sørensen, A. S. & Lukin, M. D. Faulttolerant quantum communication based on solid-state photon emitters. *Phys. Rev. Lett.* 96, 96–99 (2006).
- 50. Rozpedek, F. et al. Parameter regimes for a single sequential quantum repeater. *Quant. Sci. Technol.* **3**, 034002 (2018).
- Wehner, S., Elkouss, D. & Hanson, R. Quantum internet: a vision for the road ahead. Science 362, eaam9288 (2018).
- Najer, D., Renggli, M., Riedel, D., Starosielec, S. & Warburton, R. J. Fabrication of mirror templates in silica with micron-sized radii of curvature. *Appl. Phys. Lett.* 110, 011101 (2017).0

Acknowledgements

The authors thank Lilian Childress for fruitful discussions. The authors acknowledge financial support from the National Centre of Competence in Research (NCCR) Quantum Science and Technology (QSIT), a competence center funded by the Swiss National Science Foundation (SNF), from Swiss SNF Project grant No. 188521, from the Swiss Nanoscience Institute (SNI),

and from the Quantum Science and Technologies at the European Campus (QUSTEC) project of the European Union's Horizon2020 research and innovation program under the Marie Sklodowska-Curie Grant Agreement No. 847471.

Author contributions

V.Y. and Y.F. assembled the setup and carried out the experiments. V.Y. and B.J.S fabricated the sample, with help from A.C. V.Y. and Y.F. developed the theoretical models and analyzed and interpreted the data. Y.F., P.M., and R.J.W. provided guidance and supervised the project. V.Y., Y.F., and R.J.W. wrote the manuscript with input from all the authors.

Competing interests

The authors declare no competing interests.

Additional information

Supplementary information The online version contains supplementary material available at https://doi.org/10.1038/s41534-024-00915-9.

Correspondence and requests for materials should be addressed to Yannik Fontana

Reprints and permissions information is available at http://www.nature.com/reprints

Publisher's note Springer Nature remains neutral with regard to jurisdictional claims in published maps and institutional affiliations.

Open Access This article is licensed under a Creative Commons Attribution-NonCommercial-NoDerivatives 4.0 International License, which permits any non-commercial use, sharing, distribution and reproduction in any medium or format, as long as you give appropriate credit to the original author(s) and the source, provide a link to the Creative Commons licence, and indicate if you modified the licensed material. You do not have permission under this licence to share adapted material derived from this article or parts of it. The images or other third party material in this article are included in the article's Creative Commons licence, unless indicated otherwise in a credit line to the material. If material is not included in the article's Creative Commons licence and your intended use is not permitted by statutory regulation or exceeds the permitted use, you will need to obtain permission directly from the copyright holder. To view a copy of this licence, visit https://creativecommons.org/licenses/by-nc-nd/4.0/.

© The Author(s) 2024